Estimating dislocation density from electron backscatter diffraction data for an AZ31/Mg-0.6Gd hybrid alloy fabricated by high-pressure torsion

Thierry Baudin[1], Hiba Azzeddine[2,*], François Brisset[1], Yi Huang[3,4], Terence G. Langdon[3]

[1] Université Paris-Saclay, CNRS, Institut de chimie moléculaire et des matériaux d'Orsay, 91405 Orsay, France
[2] Laboratory of Materials and Renewable Energy, Faculty of Sciences, Mohamed Boudiaf University, 28000 M'sila, Algeria
[3] Materials Research Group, Department of Mechanical Engineering, University of Southampton, Southampton SO17 1BJ, UK
[4] Department of Design and Engineering, Faculty of Science and Technology, Bournemouth University, Poole, Dorset BH12 5BB, UK

* Corresponding author: Pr. Hiba Azzeddine, hiba.azzeddine@univ-msila.dz

Abstract

The Geometrically Necessary Dislocation (GND) density was estimated from Electron Backscatter Diffraction (EBSD) data for an AZ31/Mg-0.6Gd (wt.%) hybrid material fabricated by high-pressure torsion (HPT) at room temperature through an equivalent strain range of ε_{eq} = 0.3-144 using Kernel Average Misorientation (KAM) and the Nye tensor approaches. The results show that generally the GND densities are significant at the beginning of the deformation (ε_{eq} = 0.3) and decrease in both alloys when ε_{eq} increases. The Mg-0.6Gd alloy exhibits a lower GND density due to rapid dynamic recrystallization. These results were compared to the GND densities measured in AZ31 and Mg-0.6Gd mono-materials processed separately by HPT under the same experimental conditions. In these mono-materials the GND densities increase with increasing equivalent strain up to 7 and then decrease with further straining. The Mg-0.6Gd and AZ31 regions of the hybrid material exhibit higher GND densities than the mono-materials particularly at low strain where the disc thickness and the bonding of the AZ31/Mg-0.6Gd interfaces cause more deformation heterogeneity in the hybrid material. It is shown that the GND density evolution as a function of ε_{eq} has the same tendency for the KAM and the Nye approaches but the average values are significantly higher with the Nye approach. An analysis suggests that the Nye approach overestimates the GND density of the Mg-based alloys.

Keywords: Dislocation density; Electron Backscatter Diffraction; High-pressure torsion; Hybrid metal; Magnesium.

1. Introduction

AZ31 (Mg-3Al-1Zn, wt.%) is a lightweight alloy having a low density, high strength and biodegradability which could be used as a potential candidate to diminish the weight of certain pieces in the aerospace and automotive industries or as a biodegradable implant in biomedical applications [1-5]. Recent research shows also that it has a potential for use in biodegradable Mg batteries [6]. However, its industrial applications tend to remain limited because it suffers from poor ductility and a rapid corrosion rate. Adding rare-earth elements (RE) as alloying elements has proven efficient in improving the mechanical properties of Mg-based alloys [7-11]. Moreover, it is now well established that processing through the application of severe plastic deformation (SPD), such as using high-pressure torsion (HPT), can significantly improve the mechanical properties of materials by producing ultra-fine grain microstructures [12, 13]. It was recently reported that HPT processing can be successfully used to fabricate an original hybrid material from separate discs of AZ31 (Mg-3Al-1Zn, wt.%) and Mg-0.6Gd (wt.%) alloys thereby taking advantage of the properties of each alloy [14]. The results indicate that the microstructure of the hybrid material goes through two grain refinement regimes with the first taking place during an equivalent strain range, ε_{eq}, of ~0.3–72 and the second during ε_{eq} from ~72–517 [14].

During HPT processing, deformation with or without dynamic recovery/ recrystallization produces a microstructure with a high dislocation density and a stored energy that is classically identified as the main energy of the primary recrystallization [15]. Several techniques allow an estimation of this energy such as using X-rays or neutron diffraction through diffraction peak broadening [16, 17], Vickers microhardness [18] or the EBSD technique [19].

The total dislocation density is composed of two dislocation types: statistically stored dislocations (SSD) and geometrically necessary dislocations (GND) [20]. Based on the Ashby approach, the SSD evolve from mutually trapping processes in the form of dipoles and multipoles whereas the GND are generated as extra dislocations within a Burgers circuit to maintain lattice continuity [20].

The EBSD technique allows a practical estimation of the GND density by applying the Kernel Average Misorientation (KAM) or the Nye approaches [21-26]. The KAM approach is a measure of the local grain misorientation knowing that the dislocation density is linearly dependent on this KAM value [18, 24, 25, 27]. whereas Nye's approach is based on a tensor

which combines the dislocation content on a number of slip systems into a single tensor [19, 21, 23, 26].

Accordingly, the present work has three main objectives. The first is to evaluate the evolution of the GND density in an AZ31/Mg-0.6Gd (wt.%) hybrid material fabricated by HPT at room temperature as a function of the equivalent strain. The second is to explore the effect of the bonding interface on the GND density evolution within the two alloys by comparing the measured GND densities to those estimated in HPT-processed AZ31 and Mg-0.6Gd mono-materials under the same HPT conditions. The third is to compare the KAM and Nye approaches and the influence of the EBSD parameters on the values of the GND densities.

2. Material and experimental and numerical techniques

Discs with diameters of 10 mm and thicknesses of 0.85 mm were machined from the hot-rolled AZ31 and as-cast Mg-0.6Gd alloys [14]. The AZ31 and Mg-0.6Gd discs were HPT-processed together by placing the two discs on the lower anvil with the AZ31 disc at the bottom and the Mg-0.6Gd disc at the top and then bringing the upper and lower anvils together. The AZ31/Mg-0.6Gd hybrid material was fabricated at room temperature (RT) under quasi-constrained conditions [28, 29] for numbers of HPT turns, N, of 1/4, 1/2, 5 and 10 turns. The HPT processing was performed under a pressure of 6.0 GPa with a rotational speed of 1 rpm and care was taken to ensure there was no significant slippage during the HPT processing [30]. In addition, AZ31 and Mg-0.6Gd alloys were separately processed by HPT as mono-materials under the same processing conditions.

The equivalent strain, ε_{eq}, during HPT processing depends on the radial distance (r) from the disc center and the thickness of the disc (h) following the equation [31]:

$$\varepsilon_{eq} = \frac{2\pi N r}{\sqrt{3}h} \quad (1)$$

The thickness of the hybrid and mono-material discs after HPT processing was the same (0.63 mm) due to the quasi-constrained conditions that were used during the HPT processing.

The EBSD measurements were performed near the center (r ≈ 0.2 mm) and at the mid-radius position (r ≈ 2.5 mm) of the mid-thickness of the cross-section (CD-RD) planes of the hybrid and mono-material discs where the shear reference frame is defined as the rotational direction (RD), compression direction (CD) and shear direction (SD) [14].

The EBSD data were collected from scanned areas of 40 × 40 μm^2 with a 0.1 μm step size. The grain size data were obtained using a grain tolerance angle of 5° and the minimum grain size was chosen as 5 pixels. The Orientation Imaging Microscopy OIM^{TM} software

(version 8.6.0024, 2021) was used to analyze the results and more precisely to estimate the GND density.

2.1. GND density estimation from the KAM approach

The KAM parameter permits a determination of the average misorientation between a given point and its nearest neighbors which belong to the same grain. The average misorientation θ_{KAM} is linearly linked to the GND density, ρ_{KAM}, through the expression [24, 27]:

$$\rho_{KAM} = \frac{\alpha\theta_{KAM}}{n\delta b} \quad (2)$$

where δ is the EBSD scan step size, n corresponds to the nearest neighbor which defines the size of the kernel typically taking n =1 to 3 nearest neighbors and b = 0.32 nm is the Burgers vector. The α parameter depends on the grain boundary type with α = 2 for tilt boundaries, α = 4 for twist boundaries and with α = 3 for boundaries with mixed character [32].

The average KAM values depend strongly on various EBSD parameters such as the size of the kernel (n), the EBSD step size (δ) and the threshold angle θ_{th} for excluding points originating from grain boundaries, usually taking 5° or 15° [33]. Hence, the θ_{KAM} variations with the size of the kernel and the threshold angle are evaluated in the present study, with the calculation of the average KAM values performed without including all points of the kernel.

2.2. GND density estimation from Nye's tensors

The second approach for GND density (ρ_{NYE}) calculations is based on Nye's dislocation density tensor, α_{ij}, which was described elsewhere [23] and implemented in the OIM^{TM} software. The α_{ij} tensor quantifies the content of dislocations of ξ type in the lattice defined by a Burgers vector, b_i^{ξ}, and the slip line vector, z_j^{ξ} [34]:

$$\alpha_{ij} = \sum_{\xi} \rho_{NYE}^{\xi} b_i^{\xi} z_j^{\xi} \quad (3)$$

The crystallite with dislocation density tensor components contains lattice curvature that can be determined by orientation measurements. Thus, it is necessary to define the slip systems and the corresponding Burgers vector magnitude. Table 1 shows the presets configuration of slip systems and the corresponding Burgers vector for Mg-based alloys automatically set by the OIM^{TM} software and used in the present study.

3. Results

3.1. Evolution of the KAM maps for the hybrid and mono-materials

Figure 1 shows the KAM maps near the Mg-0.6Gd/AZ31 interfaces of the hybrid material and those of the Mg-0.6Gd and AZ31 mono-materials after equivalent strain: (a, b, c) ε_{eq} = 0.3, (d, e, f) ε_{eq} = 7, (g, h, i) ε_{eq} = 72 and (j, k, l) ε_{eq} = 144, respectively. The interfaces (see the arrows) and the Mg-0.6Gd and AZ31 regions are indicated in the KAM maps of the hybrid material. The current KAM maps were obtained by considering n = 3 and θ_{th} = 5°. In addition, only points with a confidence index (CI) [35] greater than 0.2 were included thereby excluding any suspicious orientation measurements. Usually CI lies in the range from 0 to 1 where CI = 1 characterizes an excellent indexation of the Kikuchi pattern [35]. The average KAM values (θ_{KAM}) are indicated in each KAM map (see Figure 1).

From a qualitative point of view, several observations can be highlighted from Figure 1. For the hybrid material it is apparent that the KAM values of the Mg-0.6Gd region are lower than the AZ31 region. The HPT-processed disc at ε_{eq} = 0.3 exhibits already a high average KAM value indicating a high concentration of dislocations. Thereafter, the KAM value decreases with increasing strain as a consequence of grain refinement due to dynamic recrystallization (DRX). In this stage, the dislocations tend to rearrange to form high-angle grain boundaries. For the Mg-0.6Gd mono-material the KAM value increases with increasing equivalent strain up to ε_{eq} = 7 and then decreases with additional strain up to ε_{eq} = 72 and then it appears to saturate with further straining. It is interesting to note that at low strains the dislocations are localised along the grain boundaries as indicated in Figure 1b. By contrast, there is a rapid increase in the KAM value at ε_{eq} = 7 followed by a continuous decrease with further straining for the AZ31 mono-material.

It is interesting to note also that there is a large difference in the distribution of KAM values between the hybrid material and the mono-materials, especially for the Mg-0.6Gd mono-material at the low strain of ε_{eq} = 0.3. This means that the hybrid material can store more energy than the mono-materials even if the initial metallurgical states of the as-received AZ31 and Mg-0.6Gd alloys were the same in the hybrid and the mono-materials before HPT processing.

3.2. Effect of EBSD parameters on the KAM values

The effect of several EBSD measurement parameters, such as *CI*, n, and θ_{th}, on the KAM values were preliminarily studied before estimating the GND densities using the KAM and Nye approaches. For this initial study, only the results obtained for the hybrid material are now presented. Figure 2a shows the evolution of the average KAM value as a function of the

equivalent strain calculated with CI > 0.05 and CI > 0.2 (n = 3, θ_{th} = 5°), respectively. The θ_{KAM} values are higher when CI > 0.2, especially at the lowest equivalent strains. Consequently, the estimated dislocation densities will be lower with CI > 0.05, but the evolution of the average CI as a function of equivalent strain shown in Figure 2b demonstrates that the CI > 0.2 condition exhibits a better indexation of the Kikuchi pattern than the CI > 0.05 condition. Hence, it is clearly more accurate to choose the KAM values having CI > 0.2 in order to estimate the GND density.

Figures 2c and 2d present the evolution of the average KAM value as a function of the equivalent strain calculated with n = 2 and n = 3 (CI > 0.2, θ_{th} = 15°) and calculated with θ_{th} = 5° and θ_{th} = 15° (CI > 0.2, n = 3), respectively. It is readily observed that the evolution of the θ_{KAM} values as a function of ε_{eq} are similar and they are not changed significantly with either n or θ_{th}. Increasing the kernel size (n = 3) and the threshold misorientation angle (θ_{th} = 15°) causes only an increase in the KAM values and consequently the GND densities are higher under these conditions. Since the absolute dislocation density values were not determined in this investigation, the parameters CI > 0.2, n =3 and θ_{th} = 5° initially chosen in section 3.1 are now reasonably retained for further analyses.

3.3. Estimation of GND density in the hybrid material

Figure 3a shows the evolution of the GND density as a function of the equivalent strain estimated from the KAM and Nye approaches near the Mg-0.6Gd/AZ31 interfaces of the hybrid material (taken from the maps shown in Figures 1a,1d,1g, and 1i). It should be noted that the calculation of ρ_{NYE} was carried out for the maximum misorientation of 5° and 3rd nearest neighbor. It is obvious that the evolution of the GND density as a function of equivalent strain is reasonably similar in both approaches but, with reference to the GND values, the Nye approach gives a higher estimate than the KAM approach. The GND density in the hybrid material exhibits already the highest value at low strain (ρ_{NYE} = 2.1 x 10^{15} m^{-2} and ρ_{KAM} = 0.88 x 10^{15} m^{-2} at ε_{eq} = 0.3). The ρ_{KAM} decreases slowly at ε_{eq} = 7, ρ_{KAM} = 0.82 x 10^{15} m^{-2} and reaches a value of ρ_{KAM} = 0.69 x 10^{15} m^{-2} at ε_{eq} = 144. The decrease in the GND density is more visible with the Nye approach where at ε_{eq} = 7, ρ_{NYE} = 1.8 x 10^{15} m^{-2}, and it continues to decease with increasing strain to reach a value of ρ_{NYE} = 1.2 x 10^{15} m^{-2} at ε_{eq} = 144.

Figure 3b shows the evolution of the ρ_{NYE}/ρ_{KAM} ratio as a function of equivalent strain for the hybrid material. At low strains, the ρ_{NYE}/ρ_{KAM} ratio is large (2.5) and then decreases to 1.8 with increasing strain.

3.3. Comparison of GND densities in the hybrid and mono-materials

Figures 4a and 4b show the evolution of the GND density calculated based on the KAM and Nye approaches as a function of the equivalent strain in the Mg-0.6Gd and AZ31 regions of the hybrid material and the mono-materials, respectively.

As noticed earlier, the Nye approach exhibits higher GND density values than the KAM approach in the hybrid and mono-materials but, nevertheless, their evolution as a function of strain is similar. A net difference in the GND density evolution between the hybrid and mono-materials is observed at low stain (ε_{eq} = 0.3). First, the GND value of the mono-materials increases with increasing strain up to ε_{eq} = 7 and then decreases with further strain whereas the GND values of the Mg-0.6Gd and AZ31 hybrid regions exhibit the highest values already at the low strain of 0.3 and then decrease with increasing strain. In practice, the evolution and the GND density values after a strain of ε_{eq} = 72 are quite similar in both the conditions of hybrid and mono-material.

It is apparent that the HPT processing at ε_{eq} = 0.3 generated more dislocations in the hybrid regions than in the mono-materials. However, at ε_{eq} = 7 the GND density is higher in the AZ31 mono-material (ρ_{NYE} =2.4 x 10^{15} m^{-2}) than in the AZ31 hybrid region (ρ_{NYE} =1.9 x 10^{15} m^{-2}) as shown in Figure 4b. Similar to the hybrid material, the GND density is higher in the AZ31 mono-material than in the Mg-0.6Gd mono-material. This difference is attributed directly to the DRX phenomena that differ in the two alloys [14].

4. Discussion

4.1. Evolution of the GND density in the AZ31 and Mg-0.6Gd alloys

Whether examining the mono-materials or the hybrid material and using the two different approaches (KAM or Nye), the present study shows that the GND density is higher in the AZ31 alloy than in the Mg-0.6Gd alloy. This agrees with an earlier report in which a restricted DRX occurred in the AZ31 region while very rapid DRX was observed in the Mg-0.6Gd region during HPT [14].

Figure 5 shows the grain orientation spread (GOS) maps of the Mg-0.6Gd and AZ31 mono-materials after HPT processing for ε_{eq} = 0.3 and 7, respectively. The GOS approach implemented in the OIM™ software allowed the identification of dynamically recrystallized grains in which grains with GOS < 2° are considered free of strain and therefore fully recrystallized [36].

At low strains, the fraction of DRX is similar at ~20% in both alloys. Increasing the strain to ε_{eq} =7 increases the fraction of DRX to 48% for the Mg-0.6Gd alloy due to the

development of an ultrafine grain structure while the fraction of DRX slightly increases to 25% in the AZ31 alloy. A recent comparative study between HPT-processed AZ31 and Mg-0.6Gd alloys based on the evolution of microstructure, texture and mechanical properties indicated that the restriction of DRX in the AZ31 alloy is due to the presence of stable Al_8Mn_5 particles, solute drag and grain boundary strengthening [37].

Figure 4 shows that the GND densities (ρ_{KAM} and ρ_{NYE}) are higher at low strain (ε_{eq} = 0.3) in the hybrid regions than in the mono-materials. The explanation may be linked to the development of deformation heterogeneities during the HPT processing. Indeed, a bonding of the interface AZ31/Mg-0.6Gd as in Figure 6 leads to deformation heterogeneities that could increase the dislocation densities in the Mg-0.6Gd and AZ31 regions.

These microstructural heterogeneities can obviously also explain the dispersion in the dislocation density values observed in the different curves in terms of the equivalent strain.

4.3. Comparison of the GND density estimated with the KAM and Nye approaches

Although the evolutions of ρ_{KAM} and ρ_{NYE} for the hybrid and mono-materials as a function of equivalent strain are quite similar, nevertheless the Nye approach gives higher values than the KAM approach. For comparison, Table 2 presents the evolution of the dislocation density as a function of strain estimated by the KAM (ρ_{KAM}) and Nye (ρ_{NYE}) approaches as reported elsewhere for Al 1050 [38], low carbon steel and micro-alloyed steel alloys [39], respectively.

Similar to the results in the present study, ρ_{NYE} for the Al 1050 alloy is higher than ρ_{KAM} and the ratio (ρ_{NYE} / ρ_{KAM}) decreases with increasing strain [38]. By contrast, the ρ_{NYE} and ρ_{KAM} values are very close with a ratio near to 1 for low carbon steel and micro-alloyed steel alloys [39]. It is worth noting that for both alloys the calculations for the KAM and Nye approaches were not realized under the same conditions [39]. The KAM values were calculated by choosing a threshold angle of θ_{th} = 2° whereas this angle was taken equal to 5° for the Nye tensor calculation [39]. In addition, no information was given on the kernel radius value [39].

For simplicity, the differences between the KAM and Nye approaches are now discussed only for the AZ31 mono-material from the microhardness measurements. Indeed, the total dislocation density for GND and SSD can be estimated from the Vickers microhardness using the following equation [18]:

$$\rho_{Hv} = \frac{1}{13.5}\left(\frac{Hv - Hv_0}{Ma\mu b}\right)^2 \quad (4)$$

where Hv_0 = 72 for the initial state of the AZ31 alloy [14], M = 2.6 is the Taylor factor calculated from the OIM^{TM} software, a = 0.22 is a constant [18] and μ = 17 GPa is the shear modulus.

The variation of microhardness and the corresponding total dislocation density (ρ_{HV}), and the subtraction of ρ_{HV} from ρ_{KAM} (ρ_{HV}-ρ_{KAM}) and ρ_{NYE} (ρ_{HV}-ρ_{NYE}) for the AZ31 mono-material are summarized as a function of equivalent strain in Table 3.

The total dislocation density ρ_{Hv} increases with increasing strain up to ε_{eq} = 7 and decreases with further strain which is in good agreement with the evolution of the GND density (Figure 4b). The difference ρ_{Hv}-ρ_{KAM} gives a reasonable value which may correspond to the SSD density. By contrast, Table 3 shows that the ρ_{Hv}-ρ_{NYE} values appear to be negative which indicates that the ρ_{NYE} values are superior than ρ_{Hv} but this has no physical meaning and demonstrates that the Nye approach overestimates the calculation of the GND density.

An accurate GND density calculated from the Nye approach depends strongly on the choice of the EBSD step size. It was demonstrated that a good estimate of the GND density requires an EBSD step size near to the dislocation cell structure size formed throughout the applied strain [38, 40]. Otherwise, the estimated GND density values will derive from the noise associated with the step size.

In addition, the limitation of the EBSD technique at large deformation strains, as after SPD processing, and the difficulty in indexing the Kikuchi patterns due to pattern degradation can falsify the estimate of the GND density due to the lack of sufficient orientation data to calculate the lattice orientation gradient [41]. More importantly, the Nye approach appears not suitable for a dislocation estimation when materials have different Burgers vectors due to the activation of different dislocation types as in Mg-based alloys [26]. In the OIM^{TM} software used in this investigation, all 5 slip systems (Table 1) are taken into consideration during the calculations and it is not feasible to exclude a single slip system. The ρ_{NYE} values can be modified by changing the θ_{th} and n parameters. Thus, in the first place the ρ_{NYE} and ρ_{KAM} were calculated under similar conditions (θ_{th} = 5° and n = 3, see Figure 4) but choosing θ_{th} = 2° and n = 3 to calculate ρ_{NYE} gives values lower than ρ_{KAM} (with θ_{th} = 5° and n = 3, see Figure 4) such as ρ_{NYE} = 0.85, 0.63, 0.53 and 0.52 10^{15} m^{-2} after ε_{eq} = 0.3, 7, 72 and 144, respectively. While calculating ρ_{NYE} with θ_{th} =5° and n = 2 gives higher value than the Hv measurements (see Table 3): 1.58, 3.4, 2.7 and 2.4 10^{15} m^{-2} after ε_{eq} = 0.3, 7, 72 and 144, respectively. But this raises the question of whether it is necessary to perform the ρ_{NYE} and ρ_{KAM} calculations under similar conditions.

It is recognized that the KAM approach provides a better uniform distribution of the GND density [24]. Moreover, the normalized KAM parameter, $d\theta_{KAM}/dx$ where $x = nd$, was

proposed to avoid the effect of the EBSD step size and noise parameters in the following relationship [25, 42]:

$$\rho_{KAM} = \frac{\alpha}{b}\frac{d\theta_{KAM}}{dx} \quad (5)$$

This modified equation was used, for example, to calculate ρ_{KAM} for the Al 1050 alloy [38] presented in Table 2. This modified equation was not necessary in the present study since all EBSD measurements were carried out using the same EBSD step size.

It is believed that the ρ_{KAM} values may also exceed ρ_{HV} if, for example, θ_{th} = 15° is chosen. Hence, it is concluded that the KAM and Nye approaches need to be assisted by another technique such as Vickers microhardness or X-ray diffraction if an estimate of the precise dislocation density is needed.

In conclusion, therefore, the Nye approach overestimates the GND density in this study and it appears that the KAM approach is more suitable for use with deformed Mg-based alloys. Nevertheless, both approaches can be used from a semi-quantitative point of view to compare after HPT processing different metallurgical states such as the AZ31 and Mg-0.6Gd hybrid or mono-material samples.

5. Summary and conclusions

The evolution of GND density was evaluated for an AZ31/Mg-0.6Gd hybrid material and for AZ31 and Mg-0.6Gd mono-materials after HPT processing at RT for a strain range of ε_{eq} = 0.3-144 using the KAM and Nye approaches implemented in OIM^{TM} software. There are several conclusions:

- The Mg-0.6Gd alloy in the hybrid and mono-material has a lower dislocation density than the AZ31 alloy due to the occurrence of rapid DRX.
- By comparison with the mono-materials, the GND densities are more important in the hybrid material at a strain range of 0.3-7 due to the disc thickness difference and an AZ31/Mg-0.6Gd interface bonding that leads to strong deformation heterogeneities.
- The KAM approach is more appropriate for quantifying the GND density for Mg-based alloys whereas the Nye approach overestimates the GND density in the hybrid and mono-materials. Nevertheless, the evolution of ρ_{KAM} and ρ_{NYE} in terms of the equivalent strain is similar.

Acknowledgements

We thank Dr-Ing. N. Hort and Dr. D. Letzig (MagIC, Germany) and Dr-Ing. T. Al-Samman (RWTH-Aachen University, Germany) for supplying the AZ31 and Mg-0.6Gd alloys, respectively. Y. Huang and T.G. Langdon were supported by the European Research Council under Grant Agreement No. 267464-SPDMETALS.

Data Availability: The raw/processed data required to reproduce these findings cannot be shared at this time as the data also forms part of an ongoing study.

Declaration of interest statement: The authors declare that they have no known competing financial interests or personal relationships that could have appeared to influence the work reported in this paper.

References

[1] B.L. Mordike, and T. Ebert, *Magnesium: Properties — applications — potential*, Materials Science and Engineering: A 302 (2001), pp. 37-45.

[2] J. Hirsch, and T. Al-Samman, *Superior light metals by texture engineering: Optimized aluminum and magnesium alloys for automotive applications*, Acta Materialia 61 (2013), pp. 818-843.

[3] X. Li, X. Liu, S. Wu, K.W.K. Yeung, Y. Zheng, and P.K. Chu, *Design of magnesium alloys with controllable degradation for biomedical implants: From bulk to surface*, Acta Biomater 45 (2016), pp. 2-30.

[4] B. Elambharathi, S.D. Kumar, V.U. Dhanoop, S. Dinakar, S. Rajumar, S. Sharma, V. Kumar, C. Li, E.M.T. Eldin, and S. Wojciechowski, *Novel insights on different treatment of magnesium alloys: A critical review*, Heliyon 8 (2022), p. e11712.

[5] J. Song, J. Chen, X. Xiong, X. Peng, D. Chen, and F. Pan, *Research advances of magnesium and magnesium alloys worldwide in 2021*, Journal of Magnesium and Alloys 10 (2022), pp. 863-898.

[6] N. Hassanzadeh, and T.G. Langdon, *Invited viewpoint: biodegradable Mg batteries*, Journal of Materials Science 58 (2023), pp. 13721-13743.

[7] E.A. Ball, and P.B. Prangnell, *Tensile-compressive yield asymmetries in high strength wrought magnesium alloys*, Scripta Metallurgica et Materialia 31 (1994), pp. 111-116.

[8] K. Hantzsche, J. Bohlen, J. Wendt, K.U. Kainer, S.B. Yi, and D. Letzig, *Effect of rare earth additions on microstructure and texture development of magnesium alloy sheets*, Scripta Materialia 63 (2010), pp. 725-730.

[9] A. Imandoust, C.D. Barrett, T. Al-Samman, K.A. Inal, and H. El Kadiri, *A review on the effect of rare-earth elements on texture evolution during processing of magnesium alloys*, Journal of Materials Science 52 (2017), pp. 1-29.

[10] H. Azzeddine, A. Hanna, A. Dakhouche, L. Rabahi, N. Scharnagl, M. Dopita, F. Brisset, A.-L. Helbert, and T. Baudin, *Impact of rare-earth elements on the corrosion performance of binary magnesium alloys*, Journal of Alloys and Compounds 829 (2020), p. 154569.

[11] H. Azzeddine, A. Hanna, A. Dakhouche, and B. Luthringer-Feyerabend, *Corrosion behaviour and cytocompatibility of selected binary magnesium-rare earth alloys*, Journal of Magnesium and Alloys 9 (2021), pp. 581-591.
[12] A.P. Zhilyaev, and T.G. Langdon, *Using high-pressure torsion for metal processing: Fundamentals and applications*, Progress in Materials Science 53 (2008), pp. 893-979.
[13] K. Edalati, A. Bachmaier, V.A. Beloshenko, Y. Beygelzimer, V.D. Blank, W.J. Botta, K. Bryła, J. Čížek, S. Divinski, N.A. Enikeev, Y. Estrin, G. Faraji, R.B. Figueiredo, M. Fuji, T. Furuta, T. Grosdidier, J. Gubicza, A. Hohenwarter, Z. Horita, J. Huot, Y. Ikoma, M. Janeček, M. Kawasaki, P. Král, S. Kuramoto, T.G. Langdon, D.R. Leiva, V.I. Levitas, A. Mazilkin, M. Mito, H. Miyamoto, T. Nishizaki, R. Pippan, V.V. Popov, E.N. Popova, G. Purcek, O. Renk, Á. Révész, X. Sauvage, V. Sklenicka, W. Skrotzki, B.B. Straumal, S. Suwas, L.S. Toth, N. Tsuji, R.Z. Valiev, G. Wilde, M.J. Zehetbauer, and X. Zhu, *Nanomaterials by severe plastic deformation: review of historical developments and recent advances*, Materials Research Letters 10 (2022), pp. 163-256.
[14] O. Ould Mohamed, H. Azzeddine, Y. Huang, T. Baudin, P. Bazarnik, F. Brisset, M. Kawasaki, and T.G. Langdon, *Investigation of Microstructure and Texture Evolution in an AZ31/Mg–Gd Alloy Hybrid Metal Fabricated by High-Pressure Torsion*, Advanced Engineering Materials 25 (2023), p. 2201794.
[15] A. Baczmanski, K. Wierzbanowski, A. Benmarouane, A. Lodini, P. Lipiński, and B. Bacroix, *Stored Energy and Recrystallization Process*, Materials Science Forum 539-543 (2007), pp. 3335-3340.
[16] E. Schafler, G. Steiner, E. Korznikova, M. Kerber, and M.J. Zehetbauer, *Lattice defect investigation of ECAP-Cu by means of X-ray line profile analysis, calorimetry and electrical resistometry*, Materials Science and Engineering: A 410-411 (2005), pp. 169-173.
[17] A.L. Etter, T. Baudin, M.H. Mathon, W. Swiatnicki, and R. Penelle, *Stored energy evolution in both phases of a duplex steel as a function of cold rolling reduction*, Scripta Materialia 54 (2006), pp. 683-688.
[18] H. Azzeddine, Y.I. Bourezg, A.Y. Khereddine, T. Baudin, A.-L. Helbert, F. Brisset, M. Kawasaki, D. Bradai, and T.G. Langdon, *An investigation of the stored energy and thermal stability in a Cu–Ni–Si alloy processed by high-pressure torsion*, Philosophical Magazine 100 (2020), pp. 688-712.
[19] C. Fressengeas, B. Beausir, C. Kerisit, A.-L. Helbert, T. Baudin, F. Brisset, M.-H. Mathon, R. Besnard, and N. Bozzolo, *On the evaluation of dislocation densities in pure tantalum from EBSD orientation data*, Matériaux & Techniques 106 (2018), p. 604.
[20] M.F. Ashby, *The deformation of plastically non-homogeneous materials*, The Philosophical Magazine: A Journal of Theoretical Experimental and Applied Physics 21 (1970), pp. 399-424.
[21] J.F. Nye, *Some geometrical relations in dislocated crystals*, Acta Metallurgica 1 (1953), pp. 153-162.
[22] H. Gao, Y. Huang, W.D. Nix, and J.W. Hutchinson, *Mechanism-based strain gradient plasticity— I. Theory*, Journal of the Mechanics and Physics of Solids 47 (1999), pp. 1239-1263.
[23] D.P. Field, P.B. Trivedi, S.I. Wright, and M. Kumar, *Analysis of local orientation gradients in deformed single crystals*, Ultramicroscopy 103 (2005), pp. 33-39.
[24] M. Calcagnotto, D. Ponge, E. Demir, and D. Raabe, *Orientation gradients and geometrically necessary dislocations in ultrafine grained dual-phase steels studied by 2D and 3D EBSD*, Materials Science and Engineering: A 527 (2010), pp. 2738-2746.

[25] M. Kamaya, *Assessment of local deformation using EBSD: Quantification of accuracy of measurement and definition of local gradient*, Ultramicroscopy 111 (2011), pp. 1189-1199.
[26] T.J. Ruggles, and D.T. Fullwood, *Estimations of bulk geometrically necessary dislocation density using high resolution EBSD*, Ultramicroscopy 133 (2013), pp. 8-15.
[27] Y. Ateba Betanda, A.-L. Helbert, F. Brisset, M.-H. Mathon, T. Waeckerlé, and T. Baudin, *Measurement of stored energy in Fe–48%Ni alloys strongly cold-rolled using three approaches: Neutron diffraction, Dillamore and KAM approaches*, Materials Science and Engineering: A 614 (2014), pp. 193-198.
[28] R.B. Figueiredo, P.R. Cetlin, and T.G. Langdon, *Using finite element modeling to examine the flow processes in quasi-constrained high-pressure torsion*, Materials Science and Engineering: A 528 (2011), pp. 8198-8204.
[29] R.B. Figueiredo, P.H.R. Pereira, M.T.P. Aguilar, P.R. Cetlin, and T.G. Langdon, *Using finite element modeling to examine the temperature distribution in quasi-constrained high-pressure torsion*, Acta Materialia 60 (2012), pp. 3190-3198.
[30] K. Edalati, Z. Horita, and T.G. Langdon, *The significance of slippage in processing by high-pressure torsion*, Scripta Materialia 60 (2009), pp. 9-12.
[31] F. Wetscher, A. Vorhauer, R. Stock, and R. Pippan, *Structural refinement of low alloyed steels during severe plastic deformation*, Materials Science and Engineering: A 387-389 (2004), pp. 809-816.
[32] Y. Takayama, and J.A. Szpunar, *Stored Energy and Taylor Factor Relation in an Al-Mg-Mn Alloy Sheet Worked by Continuous Cyclic Bending*, Materials Transactions 45 (2004), pp. 2316-2325.
[33] S. Wroński, J. Tarasiuk, B. Bacroix, A. Baczmański, and C. Braham, *Investigation of plastic deformation heterogeneities in duplex steel by EBSD*, Materials Characterization 73 (2012), pp. 52-60.
[34] W. Pantleon, *Resolving the geometrically necessary dislocation content by conventional electron backscattering diffraction*, Scripta Materialia 58 (2008), pp. 994-997.
[35] Y. Mikami, K. Oda, M. Kamaya, and M. Mochizuki, *Effect of reference point selection on microscopic stress measurement using EBSD*, Materials Science and Engineering: A 647 (2015), pp. 256-264.
[36] J.-H. Cho, A.D. Rollett, and K.H. Oh, *Determination of a mean orientation in electron backscatter diffraction measurements*, Metallurgical and Materials Transactions A 36 (2005), pp. 3427-3438.
[37] O. Ould Mohamed, P. Bazarnik, Y. Huang, H. Azzeddine, T. Baudin, F. Brisset, and T.G. Langdon, *A Comparative Study Between AZ31 and Mg-Gd Alloys After High-Pressure Torsion*, Journal of Materials Engineering and Performance (2023).
[38] P. Chakravarty, G. Pál, and J.J. Sidor, *The dependency of work hardening on dislocation statistics in cold rolled 1050 aluminum alloy*, Materials Characterization 191 (2022), p. 112166.
[39] P. Lisiecka-Graca, K. Bzowski, J. Majta, and K. Muszka, *A dislocation density-based model for the work hardening and softening behaviors upon stress reversal*, Archives of Civil and Mechanical Engineering 21 (2021), p. 84.
[40] D.P. Field, C.C. Merriman, N. Allain-Bonasso, and F. Wagner, *Quantification of dislocation structure heterogeneity in deformed polycrystals by EBSD*, Modelling and Simulation in Materials Science and Engineering 20 (2012), p. 024007.

[41] C. Zhu, T. Harrington, V. Livescu, G.T. Gray, and K.S. Vecchio, *Determination of geometrically necessary dislocations in large shear strain localization in aluminum*, Acta Materialia 118 (2016), pp. 383-394.
[42] C. Moussa, M. Bernacki, R. Besnard, and N. Bozzolo, *Statistical analysis of dislocations and dislocation boundaries from EBSD data*, Ultramicroscopy 179 (2017), pp. 63-72.

Figure Caption

Figure 1: KAM (n = 3, θ_{th} = 5°, CI > 0.2) maps near the Mg-0.6Gd/AZ31 interfaces of the hybrid material, Mg-0.6Gd and AZ31 mono-materials after equivalent strain: (a, b, c) ε_{eq} = 0.3, (d, e, f) ε_{eq} = 7.2, (g, h, i) ε_{eq} = 72, (j, k,l) ε_{eq} = 144, respectively.

Figure 2: (a) Evolution of the average KAM as a function of the equivalent strain for the hybrid calculated with CI > 0.05 and CI > 0.2 (n = 3, θ_{th} = 5°), (b) average CI calculated with CI > 0.05 and CI > 0.2, (c) average KAM as a function of the equivalent strain calculated with n = 2 and n = 3 (CI > 0.2, θ_{th} = 5°), and (d) average KAM as a function of the equivalent strain calculated with θ_{th} = 5° and θ_{th} = 15° (CI > 0.2, n = 3).

Figure 3: (a) Evolution of the GND density calculated with the KAM and Nye approaches as a function of the equivalent strain near the Mg-0.6Gd/AZ31 interfaces of the hybrid material, and (b) evolution of ρ_{NYE}/ρ_{KAM} ratio as a function of equivalent strain.

Figure 4: Evolution of the GND density calculated with the KAM and Nye approaches as a function of the equivalent strain in (a) Mg-0.6Gd hybrid region and mono-material and (b) AZ31 hybrid region and mono-material.

Figure 5: GOS map of Mg-0.6Gd and AZ31 mono-materials after HPT processing for (a, b) ε_{eq} = 0.3 and (c, d) ε_{eq} =7, respectively.

Figure 6: Micrograph of the cross-section of the hybrid material after ε_{eq} = 3.6. White arrows show the AZ31 region fragmentation and the formation of the AZ31/Mg-0.6Gd interface.

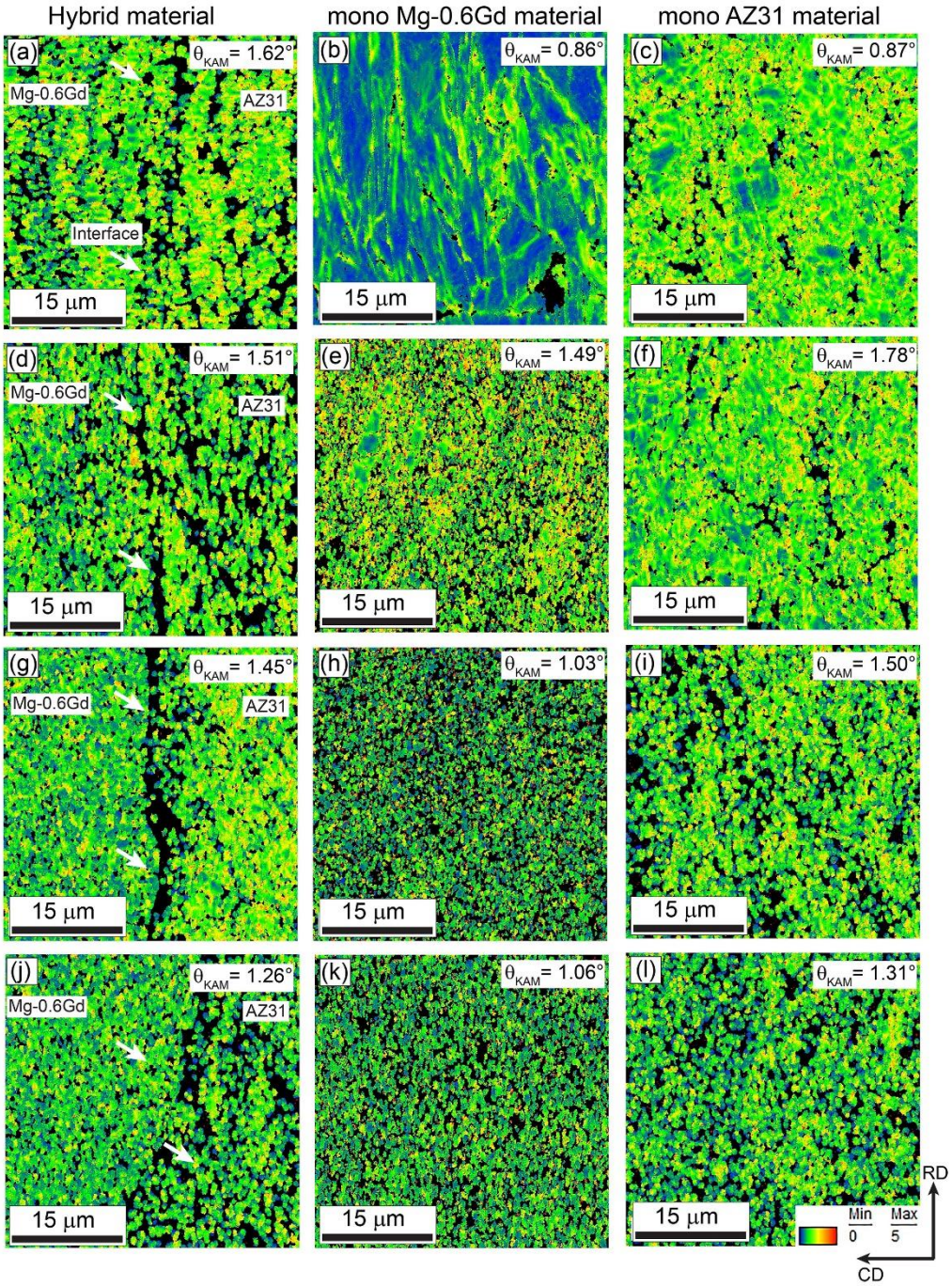

Figure 1: KAM (n = 3, θ_{th} = 5°, CI > 0.2) maps near the Mg-0.6Gd/AZ31 interfaces of the hybrid material, Mg-0.6Gd and AZ31 mono-materials after equivalent strain: (a, b, c) ε_{eq} = 0.3, (d, e, f) ε_{eq} = 7.2, (g, h, i) ε_{eq} = 72, (j, k,l) ε_{eq} = 144, respectively.

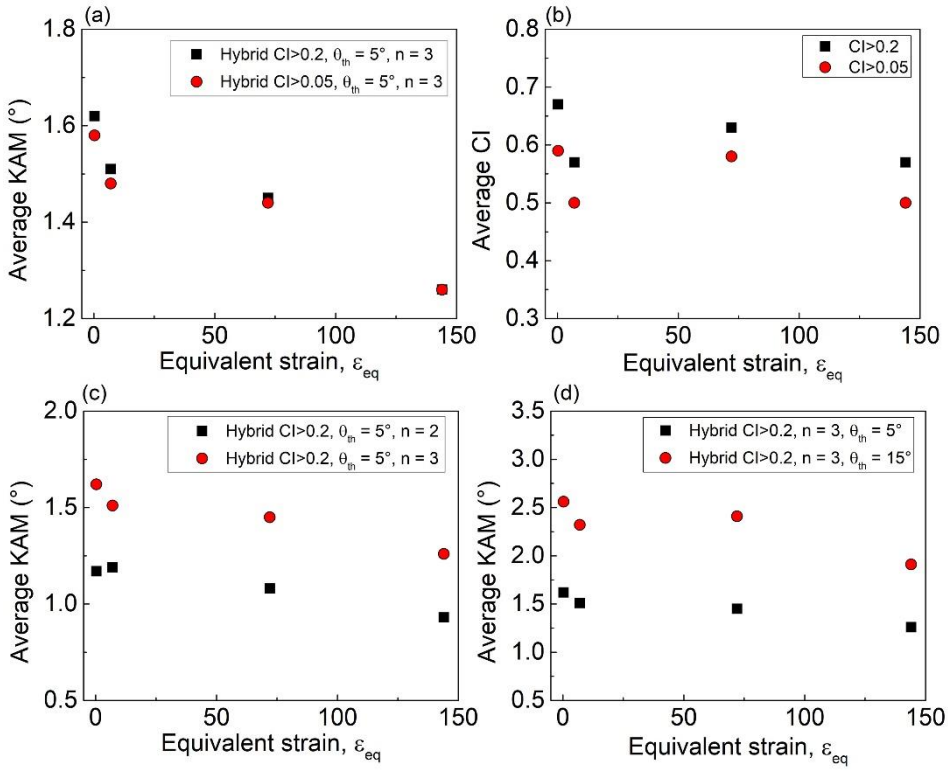

Figure 2: (a) Evolution of the average KAM as a function of the equivalent strain for the hybrid calculated with CI > 0.05 and CI > 0.2 (n = 3, θ_{th} = 5°), (b) average CI calculated with CI > 0.05 and CI > 0.2, (c) average KAM as a function of the equivalent strain calculated with n = 2 and n = 3 (CI > 0.2, θ_{th} = 5°), and (d) average KAM as a function of the equivalent strain calculated with θ_{th} = 5° and θ_{th} = 15° (CI > 0.2, n = 3).

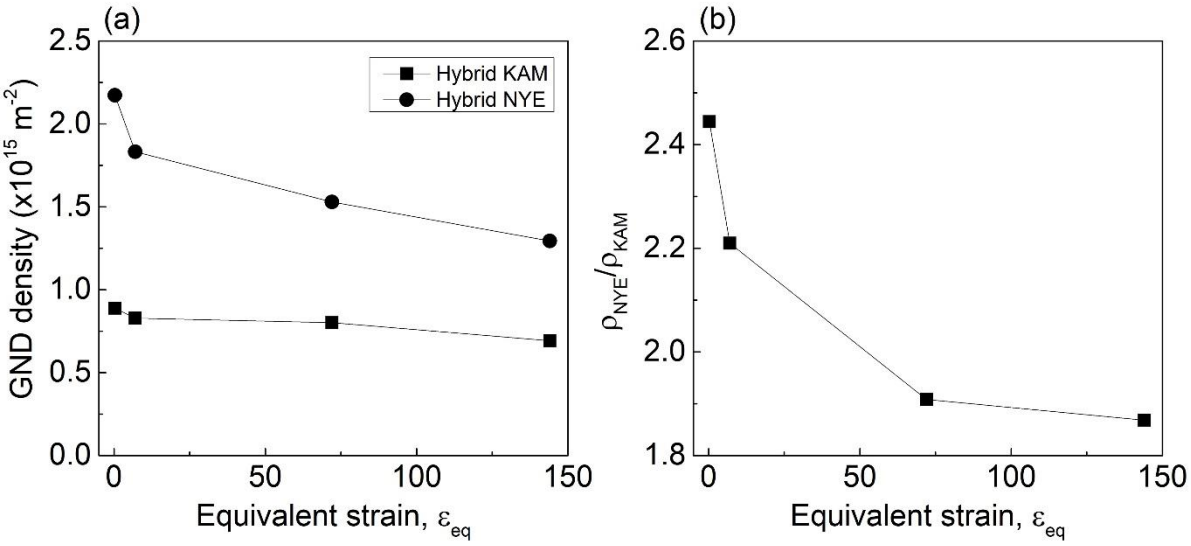

Figure 3: (a) Evolution of the GND density calculated with the KAM and Nye approaches as a function of the equivalent strain near the Mg-0.6Gd/AZ31 interfaces of the hybrid material, and (b) evolution of ρ_{NYE}/ρ_{KAM} ratio as a function of equivalent strain.

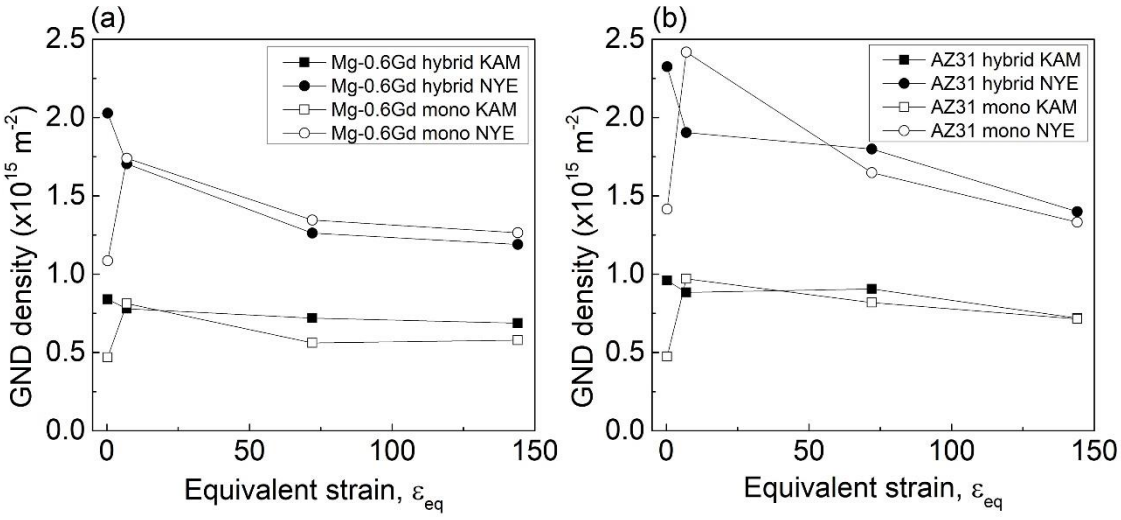

Figure 4: Evolution of the GND density calculated with the KAM and Nye approaches as a function of the equivalent strain in (a) Mg-0.6Gd hybrid region and mono-material and (b) AZ31 hybrid region and mono-material.

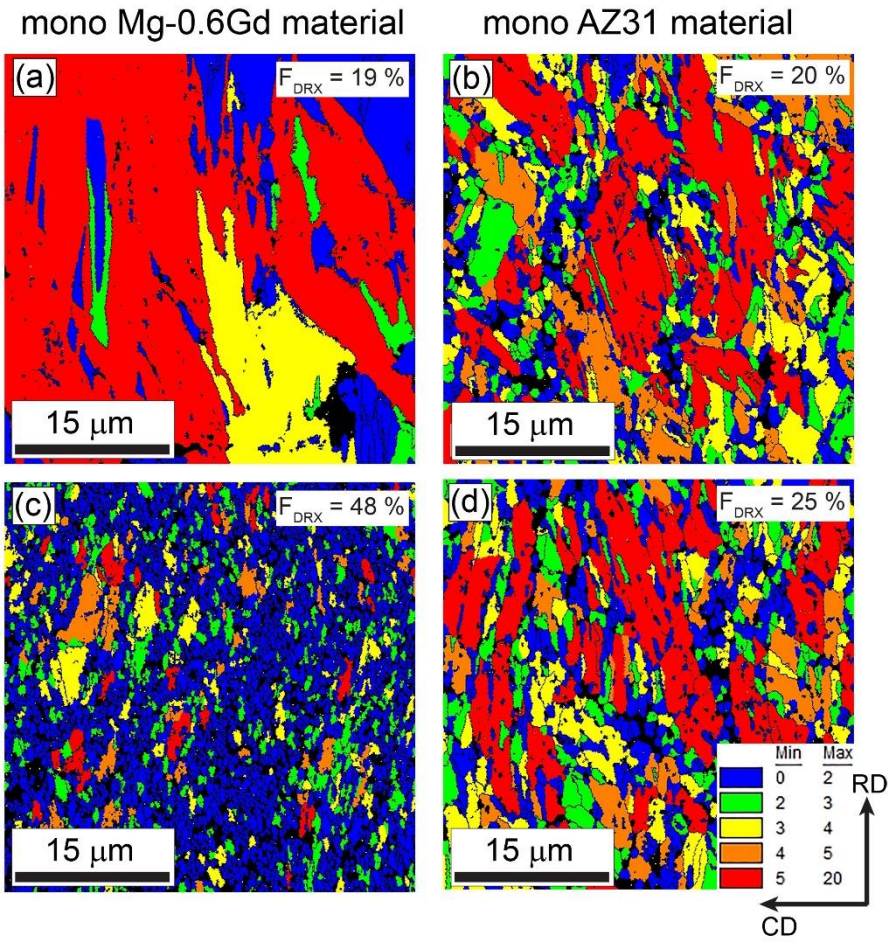

Figure 5: GOS map of Mg-0.6Gd and AZ31 mono-materials after HPT processing for (a, b) ε_{eq} = 0.3 and (c, d) ε_{eq} =7, respectively.

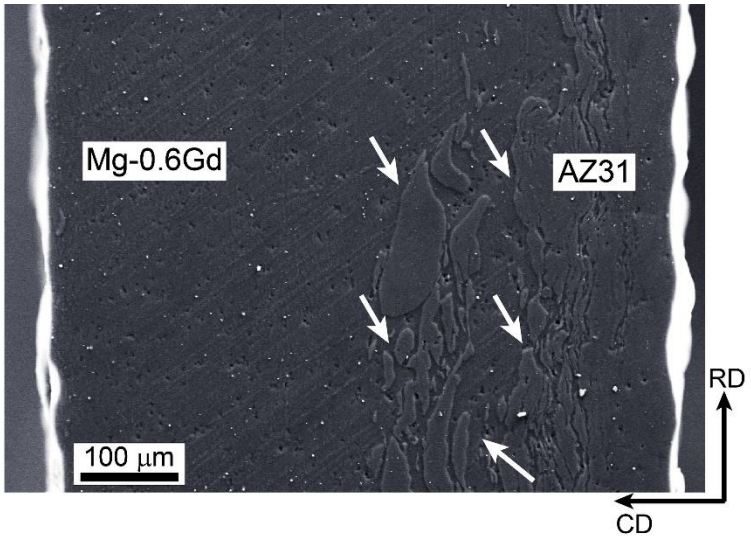

Figure 6: Micrograph of the cross-section of the hybrid material after ε_{eq} = 3.6. White arrows show the AZ31 region fragmentation and the formation of the AZ31/Mg-0.6Gd interface.

Table 1: Slip systems with the associated Burger vector for Mg-based alloys automatically set by the OIM^{TM} software.

Slip systems	Burger vector (nm)
{0001}<11$\bar{2}$0>	0.3200
{1$\bar{1}$00}<11$\bar{2}$0>	0.3200
{1$\bar{1}$01}<11$\bar{2}$0>	0.3200
{10$\bar{1}$1}<11$\bar{2}$3>	0.3063
{11$\bar{2}$1}<11$\bar{2}$3>	0.3063

Table 2. Evolution of ρ_{KAM} , ρ_{NYE} and the ρ_{NYE} / ρ_{KAM} ratio as a function of strain in Al 1050 [36], low carbon steel and micro-alloyed steel alloys [37], respectively .

Alloy	Strain	ρ_{KAM} (m^{-2})	ρ_{NYE} (m^{-2})	ρ_{NYE}/ ρ_{KAM}
Al1050 **[36]**	0.05	3.04×10^{12}	2.72×10^{13}	8.95
	0.6	6.70×10^{13}	7.14×10^{13}	1.07
	1	8.53×10^{13}	1.14×10^{14}	1.34
Low carbon steel **[37]**	0.07	2.33×10^{14}	2.29×10^{14}	0.98
	0.14	2.49×10^{14}	2.43×10^{14}	0.98
	0.27	2.86×10^{14}	2.70×10^{14}	0.94
Microalloyed steel **[37]**	0.07	2.18×10^{14}	2.08×10^{14}	0.95
	0.14	2.39×10^{14}	2.30×10^{14}	0.96
	0.27	2.90×10^{14}	2.71×10^{14}	0.93

Table 3. Evolution of *HV*, ρ_{HV}, ρ_{HV}-ρ_{KAM} and ρ_{HV}-ρ_{NYE} as a function of equivalent strain for the AZ31 mono-material.

Equivalent strain ε_{eq}	Hv (MPa)	ρ_{Hv} ($\times 10^{15}$ m^{-2})	ρ_{Hv}-ρ_{KAM} ($\times 10^{15}$ m^{-2})	ρ_{Hv}-ρ_{NYE} ($\times 10^{15}$ m^{-2})
0.3	966	0.56	0.09	-0.85
7	1060	1.03	0.06	-1.38
72	1020	0.82	0.01	-0.82
144	1000	0.73	0.02	-0.60